AERODYNAMIC TESTING OF HELICOPTER NOVEL AIR INTAKES

F. Knoth, C. Breitsamter
Chair of Aerodynamics and Fluid Mechanics, Technical University of Munich

Abstract

Aerodynamic engine integration with respect to emission reduction is one key issue of rotorcraft design in classical transport missions. This paper deals with experimental investigations and aerodynamic optimization of engine side air intakes of a lightweight helicopter aiming to improve aerodynamic engine integration. For this purpose, comprehensive wind tunnel tests are performed on a novel full scale model of a helicopter fuselage section at the Chair of Aerodynamics and Fluid Mechanics of the Technical University of Munich (TUM-AER). To simulate engine mass flow rates corresponding to realistic helicopter operation conditions the new wind tunnel model incorporates a duct system, venturi meter and a radial fan. A rake of 5-hole pressure probes is employed to obtain a total pressure ratio and distortion coefficient as aerodynamic evaluation parameters at the Aerodynamic Interface Plane (AIP). For different air intake variants, namely a "static" side intake, a "semi-dynamic" side intake as well as a "dynamic" side intake including a scoop, significant trends in dependence of mass flow rate and freestream velocity are determined. Based on the results of three baseline variants, retrofit geometric solutions are developed such as a rear spoiler and an inlet guide vane, which fit the baseline 2 intake geometry. The best retrofit solutions are presented and their aerodynamic characteristics are compared to the baseline variants.

1 Nomenclature

A cross section

c_p pressure coefficient

DC_{60} total pressure distortion coefficient

$\dot{m}$ mass flow rate

p static pressure

q dynamic pressure

S curve length coordinate

T static temperature

U velocity

W/T wind tunnel

X X-coordinate

Y Y-coordinate

Z Z-coordinate

Δ difference

η total pressure ratio

ρ air density

θ circumferential angle in AIP

Subscripts

AIP Aerodynamic Interface Plane

$corr$ corrected value

ISA ISA conditions at sea level

low lowest value of 60° sectors in AIP

max maximum value

$norm$ normalized value

Ref value for baseline variant one without intake grid at the operation condition $U_\infty/U_{\infty,max} = 0, \quad \dot{m}_{corr}/\dot{m}_{corr,max} = 0.79$

rel relative

t total

∞ = ambient condition

2   Introduction

The CleanSky initiative was launched by the European Union together with the European aerospace industry with the purpose to reduce emissions of air transport including helicopter configurations. Especially, a typical lightweight utility helicopter is addressed. In this respect, besides aerodynamic fuselage shape optimization, Ref. [1], also the aerodynamic optimization of engine installation helps to foster fuel-efficient engine operation thus decreasing emissions, Ref [2]. The work presented in this paper is part of the ATHENAI (Aerodynamic Testing of HElicopter Novel Air Intakes) project. This project belonged to the Green RotorCraft 2 (GRC2) sub-project within the Clean Sky JTI (Joint Technology Initiative). Within the ATHENAI project engine air intake concepts have been investigated in two wind tunnel campaigns. For this aim, a new full scale model of a helicopter fuselage section has been designed which allows for the modular exchange of single model components, such as the intake cowling part or the engine plenum chamber. In the first measurement campaign, for three baseline intake variants, , namely a "static" side intake, a "semi-dynamic" side intake as well as a "dynamic" side intake including a scoop, a sound database has been created, including engine entry parameters evaluated in the AIP (Aerodynamic Interface Plane) by means of a circumferentially adjustable 5-hole pressure probing system. Based on the testing results of the first wind tunnel campaign, see Ref. [3], retrofit modifications such as rear spoiler and an inlet guide vane have been investigated in the second wind tunnel campaign. In order to find the optimal combination of rear spoilers and the inlet guide vane's position, an extensive study of different combinations has been conducted. In this paper selected results are shown.

3   Wind tunnel setup

The investigations are conducted in the subsonic Göttingen-type wind tunnel facility A of TUM-AER, which is shown in Fig. 1. The measures of the atmospheric wind tunnel's open test section are: $1.8\,m \times 2.4\,m \times 4.8\,m$ (height x width x length). In open test section operation the maximum velocity is $U_\infty = 65\,m/s$. The free stream turbulence intensity is below 0.4 %. The uncertainty in the mean velocity distribution in time and space is below 0.7 %. The uncertainty in free stream direction is less than 0.2° and static pressure variations are below 0.4 %.
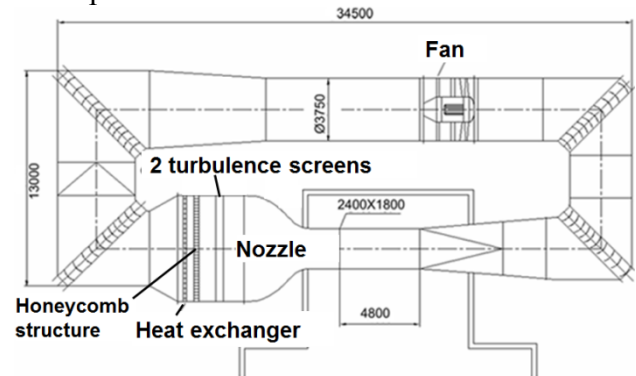

Fig. 1. Wind tunnel A facility of TUM.

Fig. 2 gives an overview of the wind tunnel model integration including all subsystems and the adjacent W/T components. In Table 1 all components are given, Ref. [3].
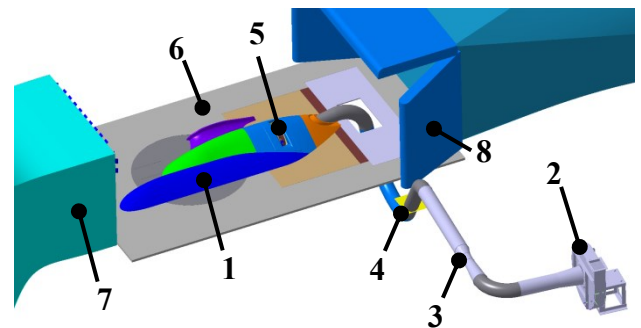

Fig. 2. Overview of the wind tunnel setup.

1	ATHENAI wind tunnel model
2	Radial fan
3	Venturi meter
4	Duct system
5	Air intake section
6	W/T floor
7	W/T nozzle
8	W/T collector

Table 1: Components of wind tunnel model and test set-up.

3.1 Wind tunnel model

A full scale model has been tested to fulfil local Mach and Reynolds number similarities. The outer geometry of the W/T model is a fuselage part model. The influence of the tail section on the upstream intake flow field is small. In fast level flight, the main rotor influence and the rotor downwash are also small for the intake region. The outer geometry is smoothened which means that antennas, rivets, screws and other small geometric details of the cabin and cowling are not reproduced. The intake and engine foreign object damage grids that have a significant impact on the local intake flow field are included.

To avoid a constriction of the freestream flow field in the vicinity of the nozzle exit and collector entry, the overall model size in the main stream direction is limited. For a reduction of blockage effects below a moderate level of $7 - 8\%$, a reduction of the model height is also desirable. Therefore, a truncated section of the cabin and cowling is tested to meet the spatial restrictions, as shown in Fig. 3 in front view.
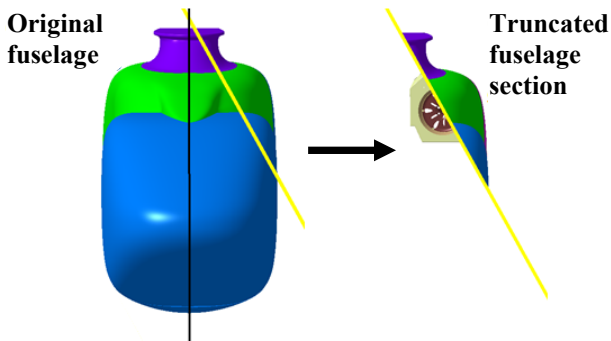

Fig. 3. Truncation of fuselage in front view.

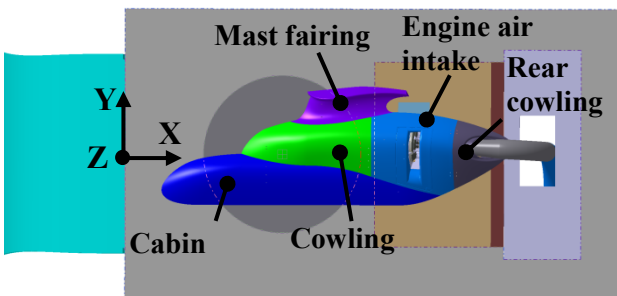The outer wind tunnel model components are presented in Fig. 4.

Fig. 4. Outer W/T model components.

Additionally, the global coordinate system is depicted. The point of origin is situated on the

bottom of the wind tunnel nozzle in its symmetry plane.

In Fig. 13, the inner model components are shown. The engine plenum chamber (EPC) is connected to the inside of the engine air intake (EAI). The plenum chamber embeds the engine intake duct (EID) which is a nozzle leading to the aerodynamic interface plane (AIP). In the real helicopter, the AIP is situated directly upstream of the compressor.

3.2 Engine mass flow simulation

The engine mass flow has a substantial effect on the flow characteristics upstream of the AIP. Therefore, in correspondence to inflight operation conditions suitable mass flow rates are reproduced in the wind tunnel. To achieve this aim, a radial fan is connected to the internal components of the model via a duct system, including two bends and a flexible tube element, see Fig. 2. For the measurement of mass flow rates, a venturi meter is integrated in the duct system, as shown in Fig. 5. The rotation speed of the fan is used to adjust mass flow rates.
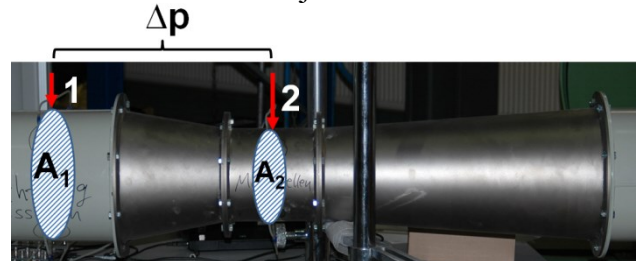

Fig. 5. Venturi meter, measurement plane 1 and 2.

A corrected mass flow rate is adjusted as defined in eq. (1) which ensures Mach number similarity for the W/T investigations compared to real flight conditions, independent of the ambient conditions, resulting from weather and height, Ref. [4].

$$\dot{m}_{corr} = \dot{m}\sqrt{\frac{T_t}{T_{ISA}}}\frac{p_{ISA}}{p_t} \tag{1}$$

$T_{ISA} = 288.15$ K and $p_{ISA} = 101325$ Pa are the ISA ambient conditions at sea level. Furthermore, T_t and p_t are the total temperature and total pressure measured at the wind tunnel nozzle exit, representing the total ambient flight conditions. Four different mass flow rates are

defined as a function of W/T freestream velocity, as shown in Fig. 6. Power requirements lead to the curve progression of the mass flow rates 1 – 3 whereas mass flow rate 4 is defined as a constant maximum mass flow rate.
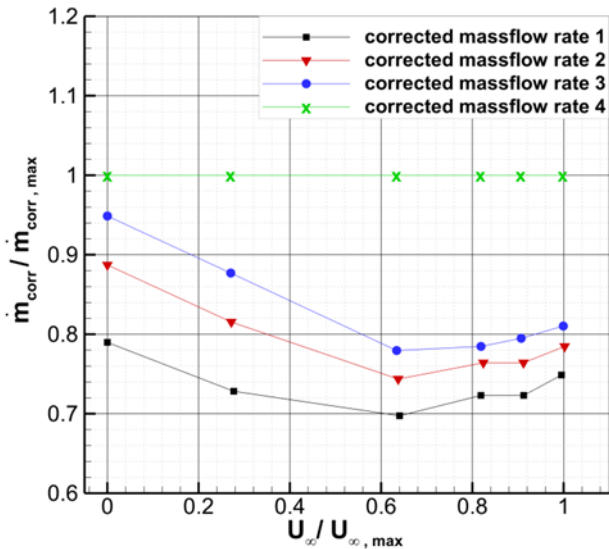

Fig. 6. Specified relative mass flow rate $\dot{m}_{corr}/\dot{m}_{corr,max}$ **as function of specified relative freestream velocity ($U_\infty/U_{\infty,max}$).**

4   Geometric Configurations

4.1   Baseline geometric variants

First, an overview of the baseline intake geometries tested in the first W/T campaign is given, as shown in Fig. 7, Ref [3].
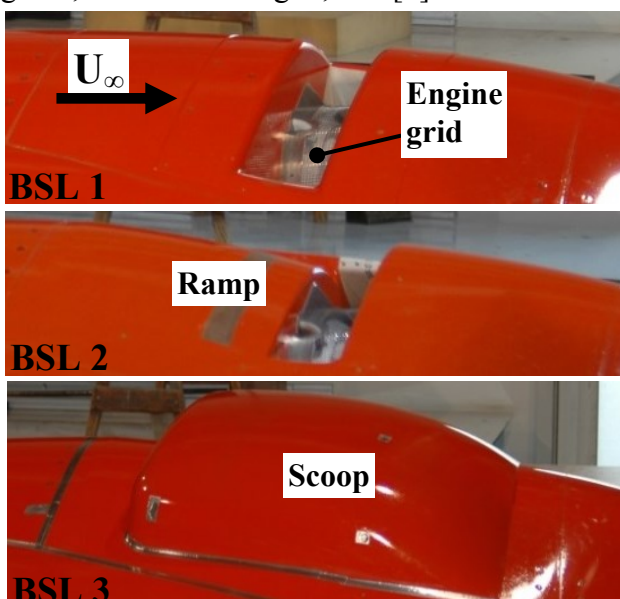

Fig. 7. Three baseline intake geometries.

Baseline variant 1 (BSL 1) is a static side intake. The baseline intake variant 2 (BSL 2) is developed as a "semi-dynamic" intake. To improve dynamic pressure recovery upstream of the intake opening, a ramp is included. The third baseline air intake (BSL 3) features the same cowling geometry of BSL 2 and an additional scoop. All three intakes exhibit an area-contraction from the intake opening to the engine face, which greatly helps to achieve low loss in hover flight conditions, Ref. [2].

Furthermore, two baseline engine plenum chamber versions (EPC) are tested, see Fig. 8. The BSL 2 variant of the EPC features an overall rounded shape compared to the BSL 1 variant. In the following, the combination of the BSL 1 intake with the EPC 1 is only referred to as "BSL 1". In analogy, "BSL 2" denotes the combination of the BSL 2 intake and EPC 2. At last, "BSL 3" names the combination of the BSL 3 intake and EPC 2.
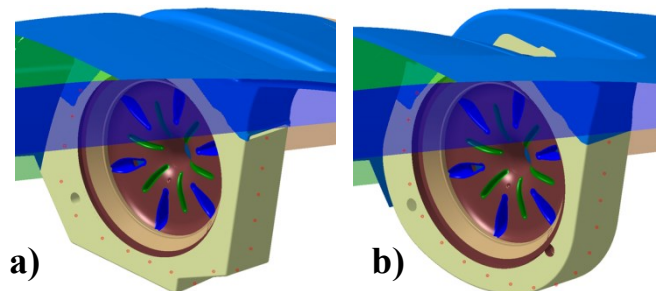

Fig. 8. a) baseline 1 engine plenum chamber, EPC 1

b) baseline 2 engine plenum chamber, EPC 2.

4.2   Modified baseline geometries

In addition to the baseline geometries investigated in [3], some geometrical modifications have been applied before testing retrofit geometries. These are described in the following. Therefore, the modified baseline geometries "BSL 1 mod", "BSL 2 mod" and "BSL 3 mod" are the new references for the retrofit geometric variants investigated as part of this research. Two foreign object damage grids are integrated upstream of the engine entry to protect the engine. The intake grid is mounted on the cowling, as exemplarily depicted in Fig. 9 a) for the BSL 1 geometry. The cylindrical engine grid is located at the EID entry, as shown in Fig. 9 b). In contrast to the investigations

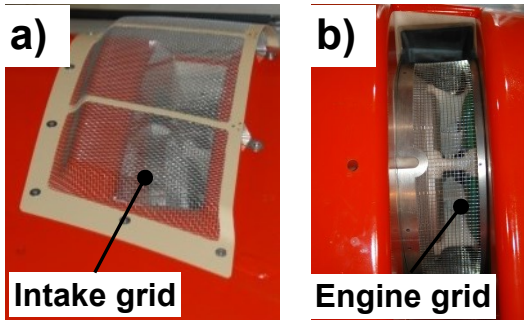presented in [3] all comparisons of this research include the intake grids.

Fig. 9. Detail of baseline intake 1 a) intake grid, b) engine grid

Furthermore, all configurations are tested including a grid mount element, which is used for the fixation of the engine grid in real flight operation. In Fig. 10 the grid mount element is presented which is located at a circumferential AIP angle position of $\theta = 270°$ (cp Fig. 13).
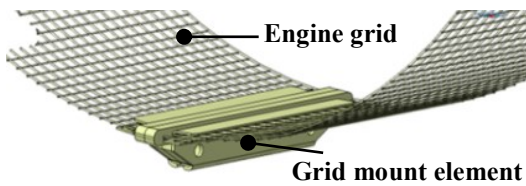

Fig. 10. Grid mount element as part of engine grid.

The first retrofit modification to the baseline geometries that has been applied is a plenum splitter, mounted at the bottom of the rounded plenum chamber, see Fig. 11.
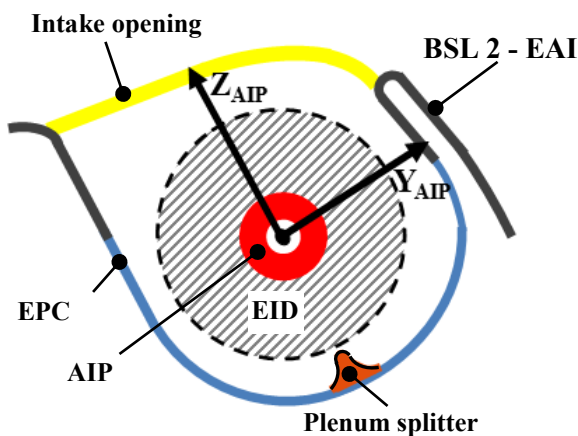

Fig. 11. Schematic cut view of modified baseline intake 2 in upstream perspective, inner components: EPC, EID, AIP and plenum splitter

It is meant to split the air flow and deflect it from a circumferential to a radial direction. It has been tested in different positions and

heights. Only the plenum splitter which led to the highest total pressures in the AIP is considered in the present work. This best plenum splitter is part of the "BSL 2 mod" and "BSL 3 mod" as well as all variants including further retrofit modifications.

4.3 Retrofit geometric variants

The evaluation of the results of the first W/T measurement campaign indicates that the BSL 2 intake variant and BSL 3 variant have a benefit compared to the BSL1 geometry at different operation points, Ref. [3]. Thus, a mixture of both configurations is desired that covers all helicopter operation points. For this purpose, further retrofit variants, namely a rear spoiler (small scoop), inlet guide vane and combination of both are investigated.

First, four different rear spoilers are tested in combination with the BSL 2 intake to assess the best combination of the height (Δh) and length (Δl) of the rear spoiler, as shown in Fig. 4. In general, an increase of the Δh also increases the cross section at the intake, thus increasing the ram effect.
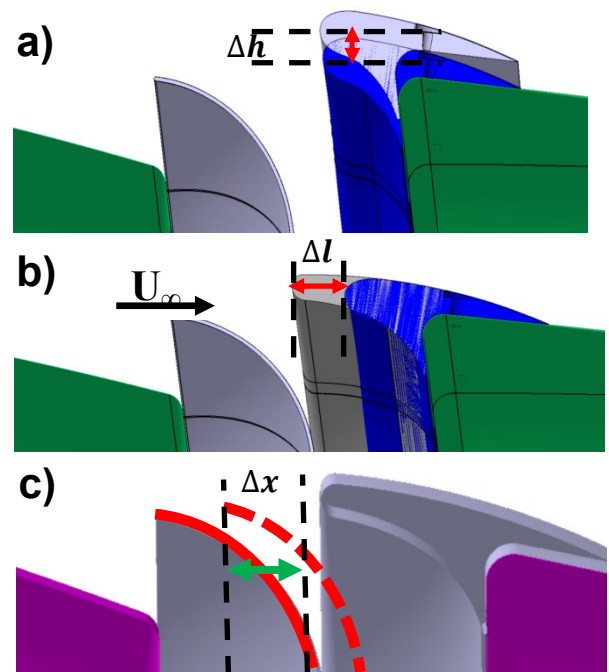

Fig. 12. Retrofit modifications: rear spoiler parameters: a) two different heights Δh, b) two different lengths Δl, c) inlet guide vane at different axial positions Δx

A decrease of the spoiler length (Δl) leads to a larger leading edge radius.

Furthermore, in the hovering condition the ingested air originated from downstream positions is deflected to a smaller degree around the rear spoiler and thus local flow separation is reduced. In the following comparisons only the best versions of all retrofit modifications are presented.

5   Measurement technique

5.1   5-hole probe measurement

For the evaluation of engine inflow conditions, total pressures and the three velocity components, namely axial, circumferential and radial velocity are obtained in the AIP, Ref. [5]. Based on these quantities total pressure losses, pressure distortion (e.g. DC60) and swirl can be obtained. For that aim, 5-hole pressure probes were embedded in a rake at four radial positions, as depicted in Fig. 13. The rake is integrated on a shaft which is driven by a stepper motor and allows for the measurement in different circumferential positions θ. The shaft is mounted in the EID front plate. The applied circumferential and radial distribution of the 5-hole probe AIP measurement locations is depicted in Fig. 13. The AIP center is chosen as point of origin. The X-axis and the engine axis are collinear. The Z-axis points at the middle of the intake opening (yellow). The Y-axis creates a right-hand system with the X- and Z- axes. The θ angles are positive in clockwise direction.
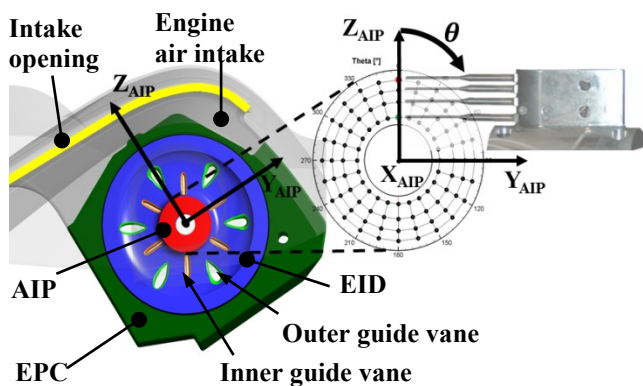

Fig. 13. Upstream view of inner components: EPC, EID, outer guide vanes in EID, inner guide vanes and AIP, schematic overview of 5-hole-probe measurement locations in the AIP, circumferentially adjustable rake comprising four 5-hole probes.

5.2   Static pressure measurement

Static pressures are measured at a total of 192 positions, 12 positions provide information about the transient pressures. In this paper, only mean surface pressures are considered. Pressure taps are situated in 8 lines along the surface of the outer geometry, as shown in Fig. 14. Additional pressure taps are located on 9 lines along the surface of the inner parts of the geometry, as shown in Fig. 15. Line 9 is situated in the mid plane of the EPC. A line is located in the circumferential positions θ = 45°, 135°, 225° and 288° on the EID front side as well as on the EID back side.
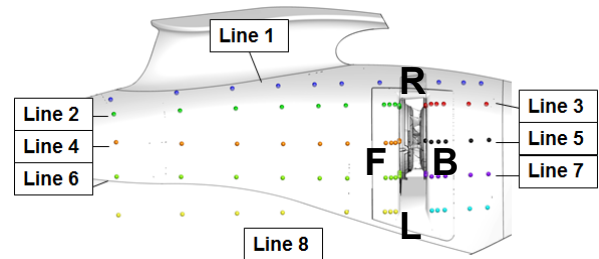

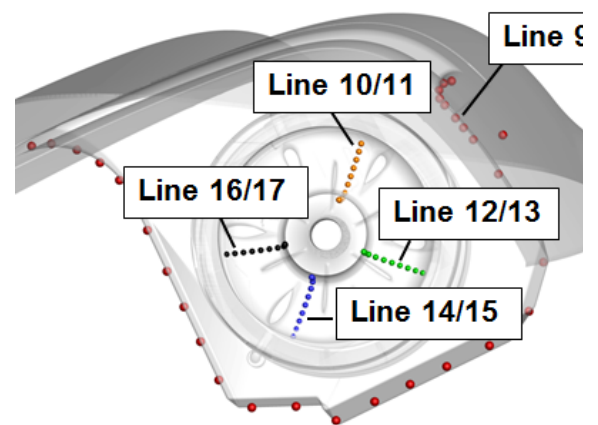Fig. 14. Top view of pressure tap positions on the outer geometry of BSL 1.

Fig. 15. Back view of pressure tap positions on the inner geometry of BSL 1.

A local curve length coordinate S is defined for each line. The coordinate S ranges from 0 to 1 and it's orientation is along the surface in the mainstream direction. Exemplarily, longitudinal sections through the model at line 2 are shown in Fig. 16 (black for BSL 1, red for BSL 2), together with the corresponding coordinate S for the surface pressure tap locations (green dots).
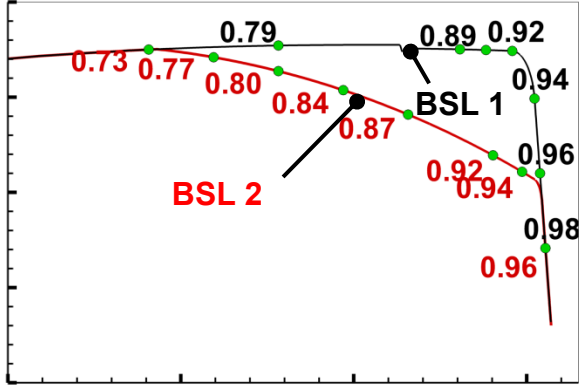
Fig. 16. Local curve length coordinate S_2 for line 2 of BSL 1, 2.

In the following, surface pressure distributions are plotted as $c_P(S) = (p(S) - p_\infty)/q_\infty$. The dynamic pressure $q_\infty = \rho_\infty/2 U_\infty^2$ is obtained with a Prandtl probe at the wind tunnel nozzle exit section.

6 Experimental Results

6.1 AIP coefficients

Two coefficients are defined for the evaluation of the aerodynamic characteristics of the intakes depending on the engine operation conditions. A normalized pressure ratio η_{norm} is defined, based on Ref. [2], to asses each intake's efficiency of the ram compression. The total pressure ratios are normalized using the total pressure ratio η_{Ref}.

$$\eta_{norm} = \frac{\bar{p}_{t,AIP}}{p_{t,\infty}} \cdot \frac{1}{\eta_{Ref}} \qquad (2)$$

Hereby, $\bar{P}_{t,AIP}$ is the mean total pressure in the AIP. $P_{t,\infty}$ is the total pressure measured at the wind tunnel nozzle exit. The total pressure distortion level in the AIP is an indicator for stable engine operation [6] and accounts for the non-uniformity of the total pressure distortion. Here, on the basis of Ref. [7], a normalized DC $_{60,norm}$ coefficient is defined as

$$DC_{60,norm} = \frac{\bar{p}_{t,low} - \bar{p}_{t,AIP}}{\bar{q}_{AIP}} \cdot \frac{1}{DC_{60,Ref}} \qquad (3)$$

The DC $_{60}$ gives the difference of the lowest average total pressure $\bar{p}_{t,low}$ sector with a circumferential extent $\theta = 60°$ and the mean total pressure $\bar{p}_{t,AIP}$ in the AIP and divides it by the mean AIP dynamic pressure $\bar{q}_{AIP}$. All DC_{60} results are normalized using $DC_{60,Ref}$.

In order to evaluate the change in aerodynamic characteristics from the baseline geometries to the modified baseline geometries, the $\eta_{norm}(U_\infty/U_{\infty,max})$ progression is presented for the baseline 2 geometry and its variants in Fig. 17. The maximum mass flow rate of $\dot{m}_{corr}/\dot{m}_{corr,max} = 1$ is chosen.
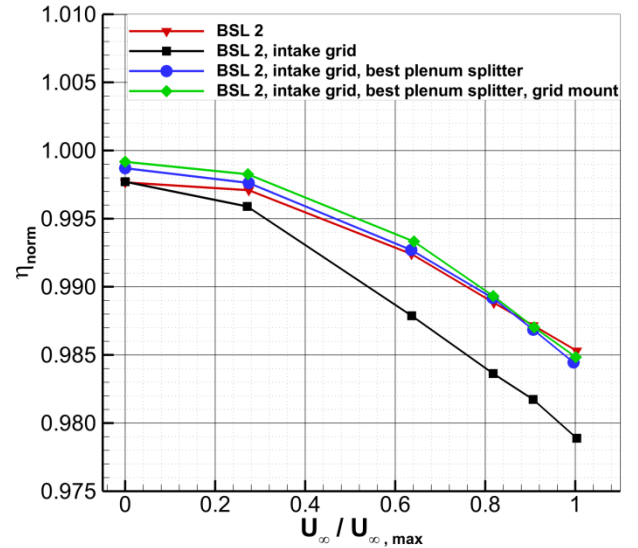

Fig. 17. Normalized total pressure ratio vs freestream velocity of the baseline 2 intake modifications for $\dot{m}_{corr}/\dot{m}_{corr,max} = 1$.

With an increase in freestream velocity, the intake grid reduces η_{norm} of the original baseline 2 intake. The maximum reduction is $\Delta\eta_{norm,rel} = -0.65\%$ for $U_\infty/U_{\infty,max} = 1$. This is due to additional total pressure losses caused by the woven wire intake grid.

With the help of the best plenum splitter, the flow at the bottom of the plenum chamber is diverted to the radial direction. Thus, due to the improved inflow direction, total pressure losses in the EID region are further reduced. Furthermore, the flow is straightened in the plenum chamber and losses caused by mixing

are reduced. Consequently, the splitter compensates the grid's negative influence on the total pressure ratio for the entire freestream velocity regime. The grid mount element does not have a significant effect. The configuration of the baseline 2 geometry including the intake grid, best plenum splitter and grid mount element is denoted in the following as "BSL 2 mod" or "modified baseline 2 variant". This applies analogously to the BSL 1 and BSL 3 variants. These modified variants are compared to the best retrofit geometric variants.

First, the η_{norm} characteristics for $\dot{m}_{corr}/\dot{m}_{corr,max} = 1$ are shown in Fig. 18. One reason for the increased η_{norm} values of the modified BSL 2 compared to the static side intake of the modified BSL 1 is the ram effect due to the ramp. The rounded baseline 2 plenum chamber including the best plenum splitter further increases total pressures. The highest relative differences of $\Delta\eta_{norm,rel,1\rightarrow2} \approx 0.5\%$ is nearly constant for $U_\infty/U_{\infty,max} > 0.6$.
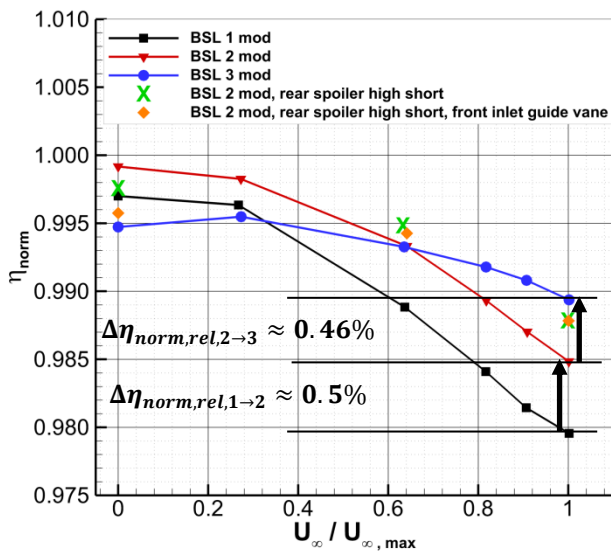

Fig. 18. Normalized total pressure ratio vs freestream velocity of the modified baseline intakes and best retrofit variants for $\dot{m}_{corr}/\dot{m}_{corr,max} = 1$.

Due to the scoop, the BSL 3 variant exhibits the best pressure recovery compared to the other baseline intakes for $U_\infty/U_{\infty,max} > 0.6$. The large relative difference of $\Delta\eta_{norm,rel,2\rightarrow3} = 0.46\%$ appears for the highest velocity. The two best retrofit modifications provide high total pressure levels. For the

highest velocities, the baseline 3 intake features slightly higher total pressures caused by the scoops' larger cross section compared to the rear spoilers. In the low velocity regime, the modified baseline 2 intake with its uncovered intake opening (cp. Fig. 12) provides the highest total pressures followed by the retrofit variant without inlet guide vane and the modified baseline 1 intake. Fig. 19 presents the levels of η_{norm} for all tested engine mass flow rates at the maximum freestream velocity.
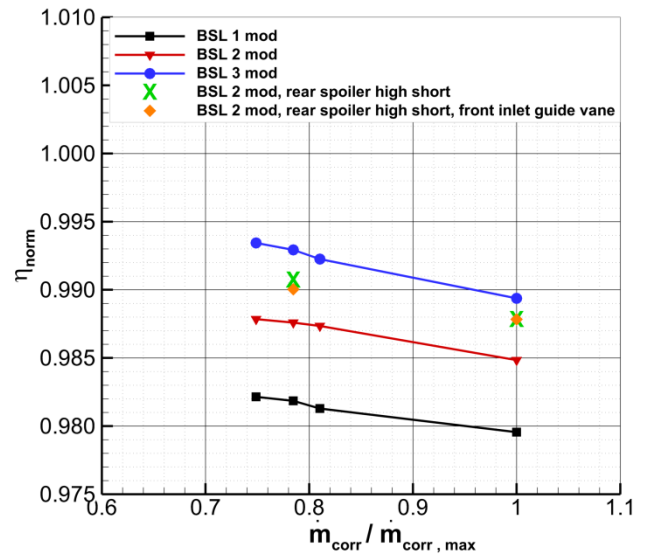

Fig. 19. Normalized total pressure ratio vs mass flow rate of the modified baseline intakes and best retrofit variants for $U_{\infty,max}$.

A linear decrease in η_{norm} with similar gradients is noticeable for all intake geometries. As depicted in Fig. 20, $DC_{60,norm}$ exhibits a very similar curve progression in the low velocity regime for the modified baseline 1 and 3 versions. Here, the distortion level is the lowest for the modified baseline 2 intake. For the higher velocities, all modified baseline variants show very similar trends. Hereby the modified baseline 1 version shows the highest and the modified baseline 3 intake the lowest levels of AIP total pressure distortion. For the entire operation range, the retrofit variant including the inlet guide vane combines the benefits of the baseline 2 and 3 intake versions. Thus, leading to the lowest variation and level of $DC_{60,norm}$. The best retrofit version without inlet guide vane features the same low level of total pressure distortion, except for the moderate velocity regime near $U_\infty/U_{\infty,max} \approx 0.6$.
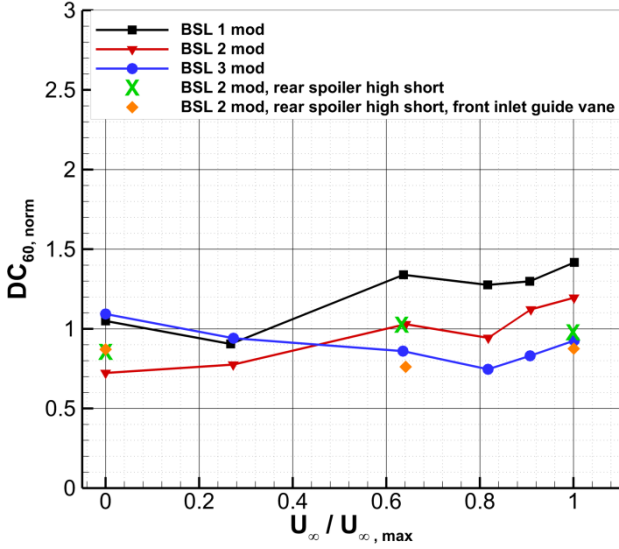
Fig. 20. Normalized distortion coefficient vs freestream velocity of the modified baseline intakes and best retrofit variants for $\dot{m}_{corr}/\dot{m}_{corr,max} = 1$.

In Fig. 21, the DC $_{60,norm}$ dependence on engine mass flow rates at a constant freestream velocity of $U_\infty/U_{\infty,max} = 1$ is presented. For all intake shapes a slight decrease in DC $_{60,norm}$ can be identified with an increase in mass flow rates. Here, the curve progression in the mass flow regime of $\dot{m}_{corr}/\dot{m}_{corr,max} < 0.8$ is very similar for the modified baseline variants. The total pressure distortion of the modified baseline 3 intake as well as the retrofit variants are nearly identical and at the lowest level of all variants.
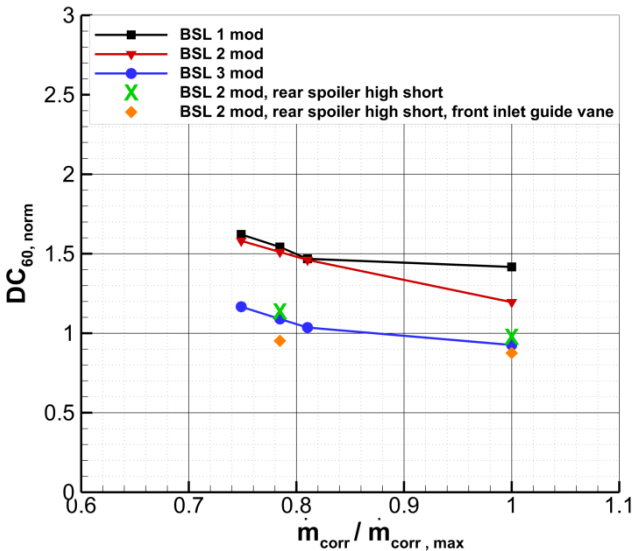

Fig. 21. Normalized distortion coefficient vs mass flow rate of the modified baseline intakes and best retrofit variants for $U_{\infty,max}$.

6.2   AIP flow field

Further investigations of η_{norm} are shown presenting the AIP distributions. The modified baseline 2 intake serves as the reference for the optimization and geometrical basis. Consequently, the corresponding data is compared to those of the two best retrofit versions. For this aim, two combinations of operation conditions of $U_\infty/U_{\infty,max}$ and $\dot{m}_{corr}/\dot{m}_{corr,max}$ are chosen for which the largest differences in η_{norm} and DC $_{60,norm}$ are noticeable. The first operation point is $U_\infty/U_{\infty,max} = 0$, $\dot{m}_{corr}/\dot{m}_{corr,max} = 1$. The η_{norm} distribution reflects the trend shown in Fig. 18. In contrast to high freestream velocities, in the low velocity regime air is ingested into the intake entry from all sides. The completely uncovered modified baseline 2 intake is therefore at an advantage compared to the partly covered configurations including a rear spoiler and inlet guide vane. These elements promote local flow separation for $U_\infty/U_{\infty,max} \to 0$. Thus, the AIP area of high η_{norm} values as well as the overall level increase in the order of c), b) and a), as depicted in Fig. 22. Generally, η_{norm} is low in the area of the AIP between $90° < \theta < 270°$. The air which enters the EID in this region has passed through several very turbulent areas of the flow field in the upstream situated plenum chamber. Therefore, its total pressure is low. High deviation from a radial inflow direction at the EID entry causes separations at the EID inner and outer guide vanes (cp. Fig. 13). Thus, further total pressure losses appear. In the top AIP region, the highest η_{norm} values are noticeable due to the fact that air from the rather undisturbed freestream flow is here particularly ingested and enters the EID in the radial direction. The regions corresponding to the highest losses are located very similarly for the three configurations. The small differences in DC $_{60,norm}$ (cp. Fig. 20) are not clearly identifiable from the η_{norm} AIP distributions.
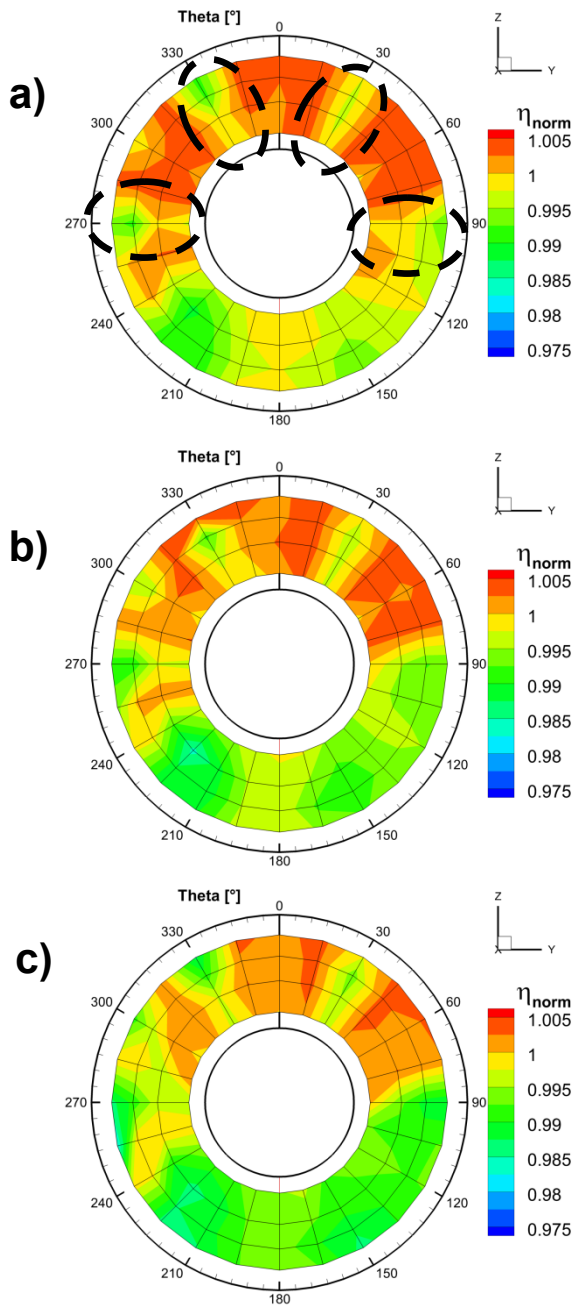
Fig. 22. Distribution of η_{norm} in AIP for a) modified baseline 2, b) modified baseline 2 + high and short rear spoiler c) modified baseline 2+ high and short rear spoiler+ front inlet guide vane, $U_\infty / U_{\infty , max} = 0$, $\dot{m}_{corr}/\dot{m}_{corr ,max} = 1$.
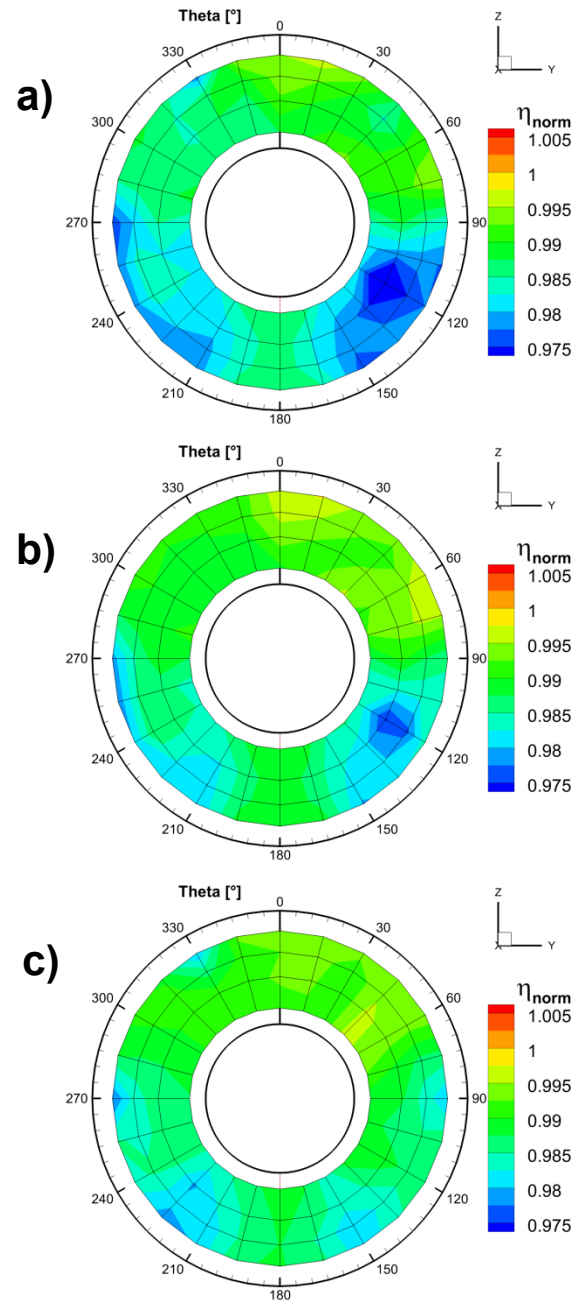

Fig. 23. Distribution of η_{norm} in AIP for a) modified baseline 2, b) modified baseline 2 + high and short rear spoiler c) modified baseline 2+ high and short rear spoiler+ front inlet guide vane, $U_\infty / U_{\infty , max} = 1$, $\dot{m}_{corr}/\dot{m}_{corr ,max} = 1$.

Especially in the upper AIP region, characterized by overall high dynamic pressures, wakes of the EID guide vanes are visible for θ = 30°, 90°, 270° and 330°. The corresponding η_{norm} deficits are shown exemplarily in Fig. 22 a) and marked with black dashed circles.

The fact that the wakes are not transported in circumferential direction shows that in this regime the radial direction is the prevailing inflow direction at the EID entry. The second operation point is characterized by $U_\infty/U_{\infty,max} = 1$, $\dot{m}_{corr}/\dot{m}_{corr,max} = 1$. The trend is reversed in the second operation point. Here, the area of low η_{norm} in the regime of 90° < θ < 170° is clearly reduced due to the rear

spoiler compared to the modified baseline 2 intake, as depicted in Fig. 23 a) and b). The inlet guide vane leads to a different distribution with even higher η_{norm} levels in this area. The location of the region of decreased η_{norm} in between $200° < \theta < 280°$ is similar for all three configurations, with the lowest level of η_{norm} for the modified baseline case 2. Overall, the trend of the η_{norm} coefficient of Fig. 18 is confirmed. The very homogeneous η_{norm} distributions for the two retrofit variants clearly reflect the decreased distortion levels in comparison to the modified baseline 2 version, compare Fig. 20.

6.3 Static pressure measurements

Selected surface pressure distributions are presented for a better understanding of the flow field in the fast forward operation condition $(U_\infty/U_{\infty,max} = 1, \dot{m}_{corr}/\dot{m}_{corr,max} = 1)$. In addition to the c_p – curves, a detail plot of the corresponding geometry is depicted. In Fig. 24, the cowling pressure distributions are given, represented by line 2 (see also Fig. 16). For the modified baseline 3 geometry, the freestream dynamic pressure can be partly converted to static pressure between $S_2 = 0.73 - 0.94$ by the use of a scoop ($c_p \approx 0 \rightarrow 0.5$), see. Fig. 24.
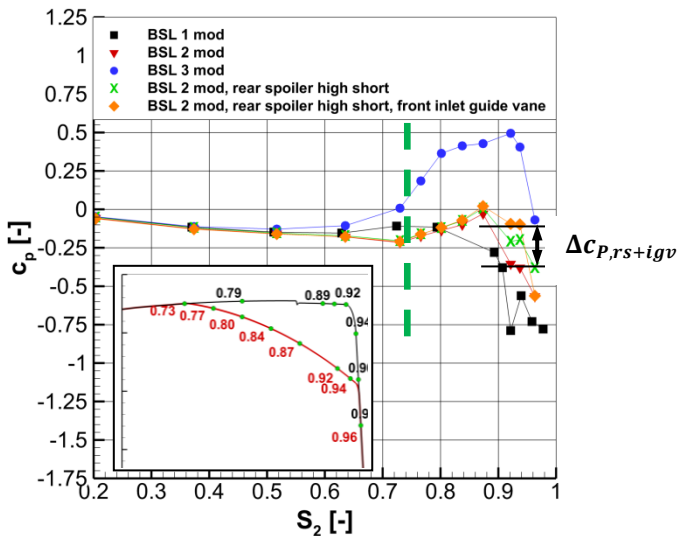

Fig. 24. Pressure distributions, line 2, modified baseline intakes and best retrofit variants, $U_\infty / U_{\infty,max} = 1$, $\dot{m}_{corr}/\dot{m}_{corr,max} = 1$.

With the ramp of BSL 2 (start of ramp shown with green dashed line in Fig. 24), an

increase in static pressure can be also achieved ($c_p \approx -0.25 \rightarrow 0$). On the other hand, no recompression is noticeable in case of the modified baseline 1 intake. Therefore, the pressure level in the separation region ($S_2 = 0.92 - 0.98$) downstream of the front inlet lip (cp. Fig. 7 and Fig. 14) is the lowest of all configurations. Directly downstream of the inlet lip, at the location $S_2 = 0.92 - 0.96$, the best rear spoiler increases the pressure level comparing to the modified baseline 2 variant by $\Delta c_{P,rs} \approx 0.16$, as illustrated in Fig. 24. The retrofit variant including the inlet guide vane leads to a pressure gain of $\Delta c_{P,rs+igv} \approx 0.27$. For all the intake variants in this comparison, the pressure differences in the plenum chamber are nearly unchanged compared to the entry face of the intake, see Fig. 25. Here, the retrofit modifications lead to an increase of static pressure over the entire plenum chamber, compared to the modified baseline 2 version. In the region of $S_9 = 0.49 - 0.53$, the effect of the splitter is clearly visible.
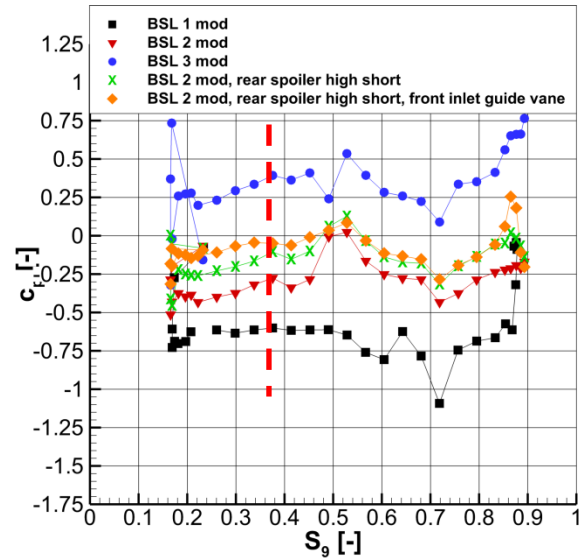

Fig. 25. Pressure distributions, line 9, baseline intakes 1-3, $U_\infty / U_{\infty,max} = 1$, $\dot{m}_{corr}/\dot{m}_{corr,max} = 1$.

The EID pressure distributions downstream of the engine plenum chamber are represented by lines 12 and 13, for which the c_p-distributions are shown in Fig. 25 and Fig. 26. These lines are located at the angle position $\theta = 135°$ and $S9 = 0.375$, respectively. The EID is identical for all intakes and symmetrical around

the engine axis. Corresponding to the EID entry pressures, the upstream engine plenum pressure values are highlighted using a red dashed line in Fig. 25.
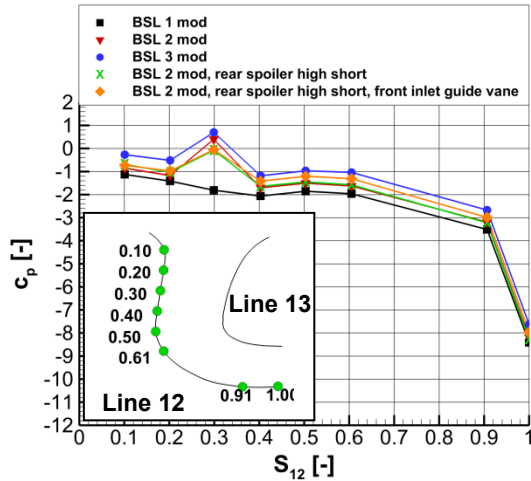

Fig. 26. Pressure distributions, line 12, modified baseline intakes and best retrofit variants, U_∞ / $U_{\infty,max}$= 1 , $\dot{m}_{corr}/\dot{m}_{corr,max}$= 1.

The pressure curve progression is very similar for all intake variants. The EID is a nozzle with a strong area contraction from entry to exit (AIP), which leads to a strong decrease in static pressure. The concave curvature of the front part of the EID (line 12) counteracts the contraction of the EID cross section, which postpones the pressure drop on this surface. In contrast, as shown in Fig. 27, the convex curvature of the back side of the EID promotes flow acceleration which leads to an earlier
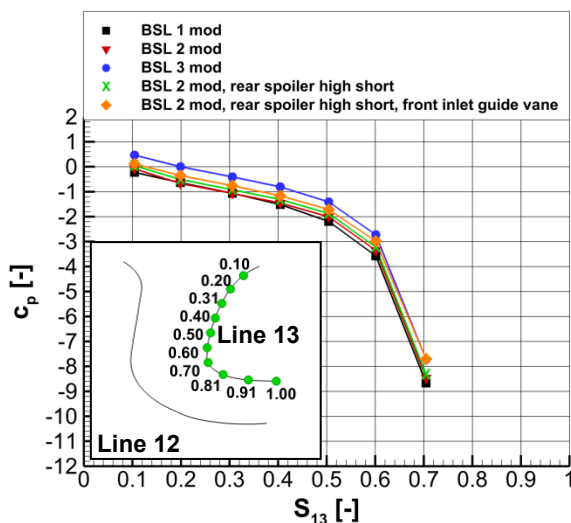

Fig. 27. Pressure distributions, line 13, modified baseline intakes and best retrofit variants, U_∞ / $U_{\infty,max}$= 1 , $\dot{m}_{corr}/\dot{m}_{corr,max}$= 1.

7   Conclusions

In this research, selected experimental results of two wind tunnel campaigns of the ATHENAI project are shown. The analysis comprises 5-hole pressure data of the AIP (Aerodynamic Interface Plane) as well as surface pressure distributions. The effect of three different engine intake and plenum chamber combinations on the normalized total pressure ratio η_{norm} and the normalized total pressure distortion coefficient DC$_{60,norm}$ is investigated. As a static intake, the baseline 1 configuration is designed to minimize total pressure losses in the engine entry face for low speed and hover flight conditions. The "semi-dynamic" baseline intake 2 features a ramp which is aimed at recovering static pressure from the freestream's dynamic pressure upstream of the intake entry. The baseline 3 intake is optimized for fast level flight conditions. For this purpose a scoop is used which provides even better dynamic to static pressure recovery. The geometries are based on the baseline configurations investigated in [3], but for the current analyses some important geometric modifications are made. The modified baseline configurations comprise an intake grid in addition to the engine grid. Furthermore, a grid mount element is integrated as well as a plenum splitter, which is part of the rounded plenum chamber of the modified baseline 2 and 3 versions only. Despite the modifications, the trends of [3] are still maintained. The investigation of η_{norm} showed that at the example of the baseline 2 intake the woven wire intake grid leads to additional total pressure losses which increase with a rise in freestream velocity. Due to the best plenum splitter, the η_{norm} deficit is compensated. The grid mount element has only minor influence on the η_{norm} coefficient. With its ramp and uncovered inlet opening, the modified baseline 2 version is a good compromise of the modified baseline 1's hover flight advantages and the modified baseline 3's fast forward flight benefits. Based on these results the modified baseline 2 variant is chosen for further optimization performed as part of the second ATHENAI project period. The

optimization includes testing of retrofit solutions for the modified baseline 2 configuration, namely rear spoilers with different heights and lengths as well as an inlet guide vane at three different positions. Two geometric configurations are chosen as the best retrofit modifications. The first version includes a short and high rear spoiler, the second one consists of the first version and an additional inlet guide vane in the front position. The retrofit version including the rear spoiler nearly reaches the η_{norm} levels of the modified BSL 2 version for low velocities as well as the modified BSL 3 versions η_{norm} levels in the high velocity regime. In the mid velocity regime both retrofit versions are better than all three baseline variants. Only for $U_\infty/U_{\infty,max} \to 0$, the additional inlet guide vane leads to additional total pressure losses. Both retrofit variants nearly reach the low DC $_{60,norm}$ values of the modified BSL 2 version for the velocity regime of $U_\infty/U_{\infty,max} \to 0$ as well as the BSL 3's low distortion levels for $U_\infty/U_{\infty,max} \to 1$, which is also valid for different mass flow rates. Thus, the most stable engine operation is possible in the entire velocity and mass flow spectrum with the retrofit versions. Generally, η_{norm} is decreased with rising mass flow rates. For the three modified baseline variants DC $_{60,norm}$ decreases with rising mass flow rates, while for the retrofit versions it is nearly constant. For both versions the test results showed that the aim of combining the benefits of baseline 2 and 3 is achieved successfully.

8   Acknowledgement

References

[1] Grawunder, M., Reß, R., Breitsamter, C., and & Adams, N. A., Flow characteristics of a helicopter fuselage configuration including a rotating rotor head, in *Proceedings of the 28th Congress of the International Council of the Aeronautical Sciences*, Brisbane, id: ICAS 2012-2.7.3, 2012.

[2] Seddon, J. and Goldsmith, E.L., *Intake Aerodynamics*, 1st edition. Collins Professional and Technical Books, 1985.

[3] Knoth, F. and Breitsamter, C., Aerodynamic Analysis of Helicopter Side Intake Variants by Full Scale Wind Tunnel Measurements, in *41st European Rotorcraft Forum*, Munich, id: ERF2015_0041, 2015.

[4] Bräunling, W. J. G., *Flugzeugtriebwerke*, 3rd ed., Springer, Berlin, 2009.

[5] Paul, A. R., Upadhyay, R. R., and Jain A., A Novel Calibration Algorithm For Five-Hole Pressure Probe, *International Journal of Engineering, Science and Technology*, Vol. 3, No. 2, 2011, pp. 89-95.

[6] Braithwaite, W. M., and Soedert, R. H., Combined Pressure and Temperature Distortion Effects, *Journal of Aircraft*, Vol. 17, No. 7, 1980, pp. 468-472. doi: 10.2514/3.57927

[7] Welte, D., Experimental Analysis of a Pitot-Type Air Intake, *Journal of Aircraft*, Vol. 23, No. 4, 1986, pp. 266-274. doi: 10.2514/3.45299

9   Contact Author Email Address

mailto:florian.knoth@aer.mw.tum.de

Copyright Statement